Title: Long-term Changes in the Coulomb Failure Function on Inland Active Faults in Southwest Japan due to East-West Compression and Interplate Earthquakes

Running Title: STRESS CHANGE IN SOUTHWEST JAPAN

Authors: Yosuke Shikakura[1,*], Yukitoshi Fukahata[2], Kazuro Hirahara[3]

Affiliations:

[1] Earthquake and Volcano Research Center, Graduate School of Environmental Studies, Nagoya University, D2-2(510), Furo-cho, Chikusa-ku, Nagoya, Japan.

[2] Disaster Prevention Research Institute, Kyoto University, Gokasho, Uji, Kyoto, Japan.

[3] Department of Geophysics, Graduate School of Science, Kyoto University, Kitashirakawa Oiwake-cho, Sakyo-ku, Kyoto, Japan.

[*]Corresponding Author: Yosuke Shikakura,

Earthquake and Volcano Research Center, Graduate School of Environmental Studies, Nagoya University, D2-2(510), Furo-cho, Chikusa-ku, Nagoya 464-8601, Japan.

(shikakura@seis.nagoya-u.ac.jp)

Key Points

Calculated viscoelastic stress changes on inland faults in southwest Japan

Nankai Trough earthquakes suppress reverse faulting and enhance strike-slip one

Inland reverse faulting increase before Nankai Trough earthquakes

Abstract

Inland earthquake activity in and around the Kinki region, southwest Japan, increases in the period from several decades before to about a decade after the occurrence of great interplate earthquakes along the Nankai Trough. To quantitatively investigate this relationship, we calculated long-term changes in the Coulomb failure function (ΔCFF) on inland active faults in this region with viscoelastic slip response functions. As sources for the change in CFF, we investigated east-west compression within the Niigata–Kobe Tectonic Zone (NKTZ), historical interplate earthquakes and interseismic locking along the Nankai Trough subduction zone, and historical inland earthquakes in this region. Among these sources, the NKTZ east-west compression is the primary cause of the long-term changes in CFF. The changes in CFF due to interplate earthquakes are mostly negative on reverse faults and positive on strike-slip faults. This result suggests that the inland reverse faulting activity mostly increases before interplate earthquakes and decreases after the earthquakes, whereas strike-slip activity is mostly suppressed before interplate earthquakes and increases thereafter. This suggestion is supported by spatiotemporal pattern of historical inland earthquakes if focal mechanisms of historical earthquakes correspond to fault mechanisms in the region. The calculated changes in CFF are usually consistent with the occurrence of historical inland earthquakes. If we use the change in shear stress instead of the change in CFF, this

consistency is enhanced, which suggests low apparent coefficients of friction in this region.

Index Terms

7223 Earthquake interaction, forecasting, and prediction

8012 High strain deformation zones

8118 Dynamics and mechanics of faulting

8164 Stresses: crust and lithosphere

7240 Subduction zones

Keywords

1: inland active fault, 2: Coulomb failure function, 3: viscoelasticity,

4: historical earthquake, 5: interplate earthquake along the Nankai Trough,

6: southwest Japan

1. Introduction

There are many inland active faults in and around the Kinki region, southwest Japan, including the Atotsugawa, Nobi, and Rokko-Awaji faults (Figure 1). In southwest Japan, the Philippine Sea (PHS) plate is subducting beneath the North American (NAM) (or Okhotsk, OKH) and Eurasian (EUR) (or Amurian, AMR) plates along the Sagami and Nankai Troughs, respectively. The movement of the inland active faults in this region is well consistent with the east-west compression observed as the Niigata–Kobe Tectonic Zone (NKTZ, *Sagiya et al.*, [2000]), which arises from the relative motion between the NAM and EUR plates [e.g., *Miyazaki and Heki*, 2001]. In addition to the east-west compression, earthquake generation on the inland faults appears to be affected by interplate earthquakes along the Nankai Trough (Figures 1 and 2). As shown by *Utsu* [1974] and *Hori and Oike* [1996], the activity of inland earthquakes in this region increases in the period from approximately 50 years before to 10 years after the occurrence of great interplate earthquakes along the Nankai Trough. The temporal relation between inland earthquakes and great interplate earthquakes has been derived from the voluminous historical records that exist for this region, where a relatively long, more continuous, and more complete set of records is available in comparison with other high-seismicity regions in the world. In addition, the distribution of inland active faults has been investigated in detail in Japan. Thus, the Kinki region is a very appropriate locality to quantitatively investigate the effect of great interplate earthquakes on the occurrence of inland earthquakes.

To understand the activity of inland earthquakes, we use the change in the Coulomb failure function (ΔCFF) [e.g., *Oppenheimer et al.*, 1988]. ΔCFF is based on the simple Coulomb failure criterion, calculated by the change in shear and normal stresses on faults with apparent coefficient of friction [e.g., *Reasenberg and Simpson*, 1992]. Several studies have already evaluated ΔCFF on inland faults in this region due to great interplate earthquakes and interseismic plate locking of the subducting PHS plate. The elastic response function was used in the computation of ΔCFF in *Hori and Oike* [1999], and the viscoelastic response function was used by a number of studies. *Pollitz and Sacks* [1997] succeeded in explaining the occurrence of the 1995 Kobe earthquake; *Hyodo and Hirahara* [2004] applied the concept of ΔCFF to five recent inland earthquakes and found that only one earthquake (1995 Kobe) was well explained. *Hirahara et al*. [2006] further evaluated stress changes on 16 inland active faults, but did not consider the NKTZ east-west compression. Moreover, in all these studies, the interaction between inland earthquakes was not considered.

In this study, we evaluate ΔCFF on inland active faults in and around the Kinki region with the viscoelastic response function. As sources for ΔCFF, we considered the NKTZ east-west compression, large interplate earthquakes, interseismic plate locking, and historical inland earthquakes. Through this evaluation, we attempt to assess how the stress changes caused by the earthquake cycle of plate subduction affect the long-term stress accumulation on inland active faults. We also investigate the validity of the ΔCFF model by comparing the calculated ΔCFF with the record of inland earthquakes. Furthermore, we attempt to quantitatively evaluate the temporal changes in the potential of occurrence of inland earthquakes.

2. Model for ΔCFF calculations

ΔCFF is defined by

$$\Delta \mathrm{CFF} = \Delta\tau_s + \mu' \Delta\sigma_n \qquad (1)$$

where $\Delta\tau_s$ and $\Delta\sigma_n$ are the changes in shear and normal stresses (positive in extension), respectively. In the following sections, $\Delta\tau_s$ and $\Delta\sigma_n$ on a certain fault are evaluated on one mechanism (strike, dip, and rake), and not on the optimally oriented plane. Here μ' is the apparent coefficient of friction and is derived from the effect of pore pressure [*Harris*, 1998]; its value is considered to be around 0.2–0.5, which we set to 0.3 in this study.

2.1. Model structure and inland active faults

In this model, we consider a horizontally stratified medium composed of an elastic lithosphere overlying a semi-infinite Maxwell viscoelastic substratum. The values of the structural parameters used in this study are as follows. In the elastic lithosphere, density $\rho = 3.00 \times 10^3$ kg/m^3, bulk modulus K = 66.7 GPa, shear modulus G = 40.0 GPa, and thickness H = 35 km. In the viscoelastic substratum, $\rho = 3.40 \times 10^3$ kg/m^3, K = 130 GPa, G = 60.0 GPa, and viscosity $\eta = 5.00 \times 10^{18}$ Pa s. The acceleration due to gravity is 9.8 m/s^2. For the geometry of the plate interface of PHS subduction, we use the CAMP model (Figure 1) of *Hashimoto et al*. [2004].

We employ quasi-static viscoelastic slip response functions with the numerical code by *Fukahata and Matsu'ura* [2006]. The effect of gravity is incorporated as the buoyant force caused by the vertical displacement on the Earth's surface.

The location, surface geometry, and mechanism of the inland active faults on which ΔCFF is evaluated are referenced from the *Earthquake Research Committee* [2005] (Table 1). The total number of the inland active faults evaluated is 80. We set the computation depth for stress change as 10 km because the hypocenters for inland earthquakes are usually located around this depth. For simplicity, the dip angles for strike-slip and reverse faults are uniformly set to be 90° and 40°, respectively, and we assume a pure strike-slip fault and a dip-slip fault, because we do not have sufficient data of the dip and rake angles at the computation depth. The exceptions are the three strike-slip faults within the Median Tectonic Line, faults I, II, and III (Figure 3). These three faults dip 40° N, from the geological structure [*Earthquake Research Committee*, 2005].

2.2. Interplate earthquakes and plate locking

In subduction zones with seismic coupling, it is thought that stick-slip behavior occurs at intermediate depths, but steady sliding occurs at shallower and deeper levels. During interseismic periods, tectonic stress caused by steady sliding accumulates in the locked intermediate depth regions and the sudden release of this stress generates interplate earthquakes. As shown by *Savage* [1983], interplate locking in the interseismic stage can be expressed as the superposition of steady plate subduction over the entire plate boundary with a back slip on the locked portion. In previous ΔCFF studies for this region [*Pollitz and Sacks*, 1997; *Hyodo and Hirahara*, 2004; *Hirahara et al*., 2006], the effect of steady plate subduction [*Sato and Matsu'ura*, 1993] has been neglected. We continue this practice.

For simplicity, we assume complete locking in the source region of the interplate earthquakes during the interseismic period. We also assume that there is no afterslip and that instantaneous locking occurs after each earthquake. Therefore, the slip deficit rate in each source region is exactly equal to the plate convergence rate, s_{rate}, in Figure 2. On the basis of the plate motion model [*Heki and Miyazaki*, 2001], the slip rate in region E (Figure 2) is decreased owing to the effect of the collision of the Izu arc (Figure 1). The slip direction in each region is uniformly set to be N308°E, following the *Earthquake Research Committee* [2001].

Historical records of interplate earthquakes along the Nankai Trough exist from the 7th century to the present (Figure 2). These records indicate that great interplate earthquakes have occurred at intervals of 90–262 years with several different temporal rupture patterns. The intervals between interplate earthquakes before the 13th century are roughly twice as long as the intervals after the 1360/1361 Shohei event; this difference is possibly because the historical records are incomplete. For the source region of the interplate earthquakes, we use the regions identified by the *Earthquake Research Committee* [2001], as shown in Figure 2. Note that in this study, we refer to the traditional "Tokai" source region, which encompasses regions C, D, and E in Figure 1. This region is named after the 1854 Ansei Tokai earthquake. Some recent studies [e.g., *Earthquake Research Committee*, 2001] have focused on a different region, E, which is referred to as the "expected" Tokai earthquake source region. The latter region was proposed by *Ishibashi* [1976] on the basis of the lack of rupture in region E during the 1944/1946 Showa event (Figure 2).

For the amount of slip in each interplate earthquake, we employ the slip predictable (SP) and time predictable (TP) models proposed by *Shimazaki and Nakata* [1980]. The SP model is based on the supposition that stress is decreased to the same level by interplate earthquakes in the same region. With the SP model, we can calculate the coseismic slip s_i at the ith earthquake for a certain region by multiplying the elapsed time since the previous earthquake ($t_i - t_{i-1}$) with the slip deficit rate s_{rate} as

$$s_i = s_{\mathrm{rate}} \, (t_i - t_{i-1}). \tag{2}$$

Here t_i is the time when the ith earthquake occurred in a certain region.

The TP model is based on the supposition that interplate earthquakes occur at the same stress level in the same region. With the TP model, we can calculate the elapsed time to the next earthquake by dividing the coseismic slip s_i by the slip deficit rate s_{rate} as

$$s_i = s_{\mathrm{rate}} \, (t_{i+1} - t_i). \quad (3)$$

To compute the slip for the last (Showa) earthquake using the TP model, we needed a value for the occurrence of the next earthquake in region ABCDE. Using the interval between the Ansei and Showa Nankai earthquakes as a constant (i.e., between 24 December 1854 and 21 December 1946, respectively), we projected that date to be 18 December 2038 and used this date in our calculations.

In this study, we employ both SP and TP models and investigate their validity by comparing the calculated ΔCFF with the record of inland earthquakes. Table 2 summarizes the slip amount for each earthquake on the basis of SP and TP models.

2.3. NKTZ east-west compression and inland earthquakes

In and around the Kinki region, east-west compression with a maximum of 1–2 × 10^{-7} year^{-1} has been deduced from the triangulation data [*Sato*, 1973]. Recently, using a GPS network denser than the triangulation network, a zone of more spatially concentrated large east-west compression (NKTZ) with a maximum of a few 10^{-7} year^{-1} has been found [e.g., *Sagiya*, 2004]. The east-west compression in the western Chubu and Kinki regions has also been estimated from inland active faults [*Kaizuka and Imaizumi*, 1984; *Tsutsumi et al.*, 2012], although the estimated rate (about 0.3 × 10^{-7} year^{-1}) is much slower than that derived from the triangulation and GPS data [*Kaizuka and Imaizumi*, 1984]. They attributed the difference to the consumption of strain by folding in the upper crust.

The NKTZ is considered to be the plate boundary between the OKH and AMR plates [*Sagiya et al.*, 2000; *Mazzotti et al.*, 2000; *Heki and Miyazaki*, 2001] or an internal deformation zone near the eastern margin of the AMR plate [*Iio et al*., 2002; *Hyodo and Hirahara*, 2003]. However, there is an agreement that the NKTZ arises from the relative motion between the OKH (NAM) and AMR (EUR) plates because the NKTZ compression is consistent with global plate motion models. The speed and azimuth of the relative motion between the OKH (NAM) and AMR (EUR) plates at (35.3°N, 136.3°E) were estimated to be 11 mm/year and N90°E by Nuvel-1A [*DeMets et al*., 1994], 30 mm/year and N103°E by REVEL 2000 [*Sella et al*., 2002], and 22 mm/year and N105°E by GSRM v1.2 [*Kreemer et al*., 2003], respectively. Note that in Nuvel-1A, the OKH and AMR plates are not separated from the NAM and EUR plates.

In calculating ΔCFF, we set the maximum compressive strain rate due to NKTZ east-west compression, $\Delta\varepsilon_{\mathrm{NKTZ}}$, to be 0.3×10^{-7} year^{-1} on the basis of the inland active fault data. The direction was taken to be N100°E. Then, the change in normal stress on the plane normal to N100°E, $\Delta\sigma_{\mathrm{NKTZ}}$, is expressed as

$$\Delta\sigma_{\mathrm{NKTZ}} = E\Delta\varepsilon_{\mathrm{NKTZ}} \tag{4}$$

where E is the Young's modulus (100 GPa), which is calculated from the structural parameters given in section 2.1. The stress accumulation rate due to NKTZ compression, $\Delta\sigma_{\mathrm{NKTZ}}$, is 3 kPa/year, which is consistent with the stress accumulation rate for "A class" inland active faults in Japan (average slip rate higher than 1 mm/year) [*Hori and Oike*, 1999]. For simplicity, the principal stress components other than $\Delta\sigma_{\mathrm{NKTZ}}$ are assumed to be zero.

As mentioned above, a continuous historical record of inland earthquakes exists for this region. On the basis of both historical records and geological surveys, some of the source faults of historically recorded inland earthquakes have been identified. This information is summarized in Table 3. In Figure 3, fault numbers (a–o) are attached to the source faults to indicate which fault is associated with each of these historical inland earthquakes in Table 3. The stress changes due to these inland earthquakes were included in our calculations. In the calculations, we assume the source region of each inland earthquake ranges from the Earth's surface to the depth of 20 km.

3. Evaluation of ΔCFF on inland active faults

3.1. ΔCFF due to NKTZ east-west compression

Calculated ΔCFF is positive for most inland active faults with values of around 1–2 kPa/year (Figure 4a). This result is consistent with the idea that inland earthquakes in this region are mainly generated by NKTZ east-west compression. Conversely, according to the standard theory of fault mechanics [*Anderson*, 1951], the strike of inland faults in this region is consistent with east-west compression: N–S trending reverse faults, NW–SE trending left-lateral strike-slip faults, and NE–SW trending right-lateral strike-slip faults (Figure 3).

However, ΔCFF is negative on some faults (faults α, β, and γ in Table 1 and Figure 4a). In the computation of ΔCFF, the value of the apparent coefficient of friction is set to 0.3. To investigate the sensitivity of the computed results to the apparent coefficient of friction, we also plot the change in shear stress ($\Delta\tau_s$), i.e., ΔCFF with the apparent coefficient of friction μ' = 0 (Figure 4b). When this is done, $\Delta\tau_s$ are positive on all the faults in the model region. To be precise, we confirmed that ΔCFF due to NKTZ compression is positive on all the faults in this region if apparent coefficient of friction μ' is less than 0.15. Such a low apparent coefficient of friction is consistent with previous studies [*Iio*, 1997; *Reasenberg and Simpson*, 1992]. Another possible explanation for low normal stress on the faults may be the activity of other faults nearby: left-lateral strike-slip motion to the west of fault α and reverse fault movement to the east of faults β and γ might reduce the normal stress on the faults α, β, and γ.

3.2. ΔCFF due to interplate earthquakes

In the previous section, we showed that the general trend of the strike of the inland active faults in and around the Kinki region is consistent with east-west compression in the NKTZ. Under the setting, we then investigate what pattern of ΔCFF is generated owing to the earthquake cycle along the Nankai Trough.

Figure 5 presents ΔCFF on inland active faults due to coseismic slips with different combinations of the source regions of interplate earthquakes; regions of interplate earthquakes are shown in the inset of each diagram. Each combination of the source regions corresponds to a historical interplate earthquake shown in Figure 2. To construct Figure 5, the amount of slip used for the calculations in each region was set to the accumulated slip deficit for 100 years. It should be noted that Figure 5b precisely corresponds to ΔCFF due to complete plate locking with elastic response functions when the sign of ΔCFF is reversed. For comparison, ΔCFF for 100 years due to the NKTZ compression is shown in Figure 5a, which is exactly the same as Figure 4a except the unit.

We can see from Figures 5a and 5b that ΔCFF due to an interplate earthquake over the entire region (A-E) has a magnitude similar to that due to NKTZ east-west compression, except for the northernmost area of the model region where the NKTZ east-west compression is dominant. However, note that ΔCFF due to interplate earthquakes is basically canceled out in the long term by the stress change due to interplate locking. In contrast, ΔCFF due to NKTZ east-west compression accumulates monotonically. Comparing Figures 5b and 5c, we can see that the slip in region E affects the easternmost area of the model region. When slip is absent in regions C and D (Figure 5d), the magnitude of ΔCFF drastically decreases on most faults except in the western part of the model region. On the other hand, the computed ΔCFF values are basically similar in Figures 5b and 5e. In other words, ΔCFF in Figure 5b is dominated by the slip in regions C and D.

It is interesting that the sign of ΔCFF due to the interplate earthquake over the entire region (A-E) changes depending on the fault type (Figure 5b); ΔCFF is negative on most reverse faults, while positive on most strike-slip faults. This arises from the general strike of the trend of inland faults, which is well consistent with east-west compression. When an interplate earthquake over the entire region (A-E) occurs, the crust of the model region basically moves to the SSE because it is mostly located NNW of the nearest source region. As a result, ΔCFF on N–S trending reverse faults decreases, while ΔCFF on NW–SE trending left-lateral strike-slip faults and NE–SW trending right-lateral strike-slip faults increases. On the other hand, for the Tonankai (Figure 5e) or Tokai (Figure 5f) earthquakes, we can see ΔCFF on the strike-slip faults in the western part of the model region decreases. This is because the crust, which is located to the WNW of the source regions, is moved to the ESE by the earthquake.

To understand the viscoelastic response, we constructed Figure 6 in which we show temporal profiles of ΔCFF due to interplate earthquakes along the Nankai Trough. Figures 6a and 6b show examples of a reverse fault (fault b in Figure 3) and a strike-slip fault (fault l), respectively. As shown in Figure 6, the effects of viscoelastic relaxation on ΔCFF are not large in comparison with the elastic change, mainly because the viscoelastic effects from regions AB and CD cancel out each other. This cancelation occurs on most faults in the model region. The viscoelastic stress relaxation can be larger than the elastic stress change in areas far away from the source regions of the earthquake; however, the effect of NKTZ east-west compression is more dominant. As shown in Figure 5, the effect of slip in region CD is generally dominant in the elastic stress changes. In terms of viscoelastic stress relaxation, however, the effect of slip in region AB is larger than that in region CD in some cases (first several decades in Figures 6a and 6b). This is because the fault areas and slip amounts of region AB are larger than those in region CD, although the distance from the model area to region AB is farther than that to region CD.

3.3. Time evolution of ΔCFF due to all sources

Figure 7 shows the time evolution of ΔCFF (black) and $\Delta\tau_s$ (red), ΔCFF(t) and $\Delta\tau_s(t)$, on the 13 inland active faults for which we have historical records of earthquake occurrences. All sources are considered in the computation of Figure 7, where the faults, slip amounts, and occurrence years of interplate and inland earthquakes are taken from the historical records (Tables 2 and 3). We set the reference year for ΔCFF(t) to 1477, the end of the Ohnin war. The Ohnin was the biggest civil war in the history of Japan and was fought mainly in and around the city of Kyoto (Figure 3), the capital of Japan at the time. After the war, historical records are much more complete. However, note that we were compelled to start the computation well before 1477 in order to take into account the effect of viscoelastic relaxation of the 1360/1361 Shohei earthquake and the subsequent interseismic locking. Interplate earthquakes before the Shohei event were not considered because their viscoelastic relaxation had almost certainly been completed before 1477.

We categorize ΔCFF(t) on the inland faults shown on Figure 7 into three basic patterns: (1) monotonic increase during most of the period (e.g., faults c, i, j, k, m, and n), (2) decrease at the time of interplate earthquakes and increase in interseismic periods due to the interplate locking and NKTZ compression (e.g., faults d, e, f, and h), and (3) increase at the time of interplate earthquakes, decrease in the post-seismic period due to the viscous relaxation and interplate locking, and then again increase due to the NKTZ compression (e.g., faults g, l, and o). In some cases, we can also recognize the effect of the stress change due to inland earthquakes (e.g., faults g, h, j, l, n, and o).

4. Validity of the ΔCFF model

4.1. Comparison with the historical earthquakes on inland faults

If an earthquake on a fault occurs when ΔCFF(t) on the fault is the highest, the earthquake is consistent with the concept of ΔCFF(t) that ΔCFF(t) reaches its maximum value immediately before fault rupture. As shown in Figure 7, for both SP and TP models, the concept of ΔCFF(t) is mostly valid in the occurrences of inland earthquakes in and around the Kinki region during the last 500 years.

In some cases, faults ruptured when ΔCFF(t) on the faults was not at the highest value. We can see from Figure 7 that for the 13 fault movements depicted, five SP model cases (d, g, k, l, and o) and four TP model cases (g, k, l, and o) behave in this way. However, when more than one fault ruptures during a single earthquake, some of the fault movements could be triggered by the dynamic effect of rupture propagation. In fact, *Mikumo and Ando* [1976] estimated that the rupture of the 1891 Nobi earthquake started at fault j and propagated to faults k and l. Although we do not have information on rupture propagation for inland earthquakes before the 1891 Nobi earthquake, similar events may have occurred. If we take this effect into account, the number of cases that do not fit the concept of ΔCFF(t) is reduced to one for both the SP and TP models (event o).

If we use $\Delta\tau_s(t)$ (solid red lines in Figure 7) instead of ΔCFF(t) as a criterion for fault rupture, a larger number of fault ruptures occur at the highest value. The number of exceptions is reduced to four for the SP model (d, g, k, and l) and three for the TP model (g, k, and l). If we consider the dynamic effect as discussed above, there are no exceptions. All fault ruptures occurred when $\Delta\tau_s(t)$ on the faults was at the highest.

4.2. Estimating the potential of inland earthquake occurrences from ΔCFF calculations

As examined in the previous section, the concept of ΔCFF(t) is mostly consistent with the historical records of earthquake occurrences in and around the Kinki region. An earthquake tends to occur when ΔCFF(t) reaches its maximum. On the basis of the concept, we can further assume that the degree to which the highest value of ΔCFF(t) on a fault is renewed during a certain period is related to the potential of earthquake occurrence on that fault during the period. We define the increment value of the highest ΔCFF(t), $\Delta \mathrm{CFF}_i(t)$, which is given by

$$\Delta \mathrm{CFF}_i(t) = \max[0, \max[\Delta \mathrm{CFF}(t_x): t - \Delta t \le t_x < t] - \max[\Delta \mathrm{CFF}(t_x): t_0 \le t_x < t - \Delta t]] \quad (5)$$

where t_0 and Δt are the reference year and time duration, respectively. Afterwards, we use $\Delta\mathrm{CFF}_i(t)$ to describe the degree to which the highest value of ΔCFF is renewed.

Figure 8 schematically illustrates the procedure to obtain superimposed and normalized $\Delta\mathrm{CFF}_i(t)$ from $\Delta\mathrm{CFF}(t)$. In this figure, we set t_0 and Δt are the year 0 and 10 years, respectively. Figure 8a shows a hypothetical profile of $\Delta\mathrm{CFF}(t)$ on an idealized reverse fault where great interplate earthquakes along the Nankai Trough repeatedly occurred. $\Delta\mathrm{CFF}(t)$ in Figure 8a is converted to $\Delta\mathrm{CFF}_i(t)$ by equation (5), as shown in Figure 8b. Then, profiles of $\Delta\mathrm{CFF}_i(t)$ in Figure 8b are superimposed for the interplate earthquakes and normalized to the total summation of $\Delta\mathrm{CFF}_i(t)$ for the interplate earthquakes. The result is shown in Figure 8c. Here, for stacking, we set the time range of the relative time to the occurrence of each interplate earthquake from −50 to +40 years. That is, we set t for superimposed and normalized $\Delta\mathrm{CFF}_i(t)$ to be every 10 years from −40 to +40 years (Δt = 10 years). In Figure 8c, the horizontal axis represents the time relative to the occurrence years of the great interplate earthquakes along the Nankai Trough. To avoid overestimation of superimposed and normalized $\Delta\mathrm{CFF}_i(t)$ for early years in an earthquake cycle, we do not use the first earthquake (the year 23) as a reference.

Figure 9 shows superimposed and normalized $\Delta\mathrm{CFF}_i(t)$ on inland active faults in the region surrounded by the thick dotted line in Figure 3. We chose this region because both the east-west compression and interplate earthquakes are important to the stress change. By taking the average of superimposed and normalized $\Delta\mathrm{CFF}_i(t)$ for all the faults in the region, we obtained dotted lines in Figure 9 (left axis). We claim that the profile of all the faults would be related to the potential of inland earthquake occurrences in this region. For comparison, we also show the superimposed and normalized increment value of the highest $\Delta\tau_s(t)$, $\Delta\tau_{si}(t)$, by solid lines. Reference time t_0 = 1477.0, the range of relative time is from −80 to +40 years. That is, we set t for the superimposed and normalized increment values to be every 10 years from −70 to +40 years. When deciding occurrence years of the interplate earthquakes, we chose only those of region CD because region CD plays a dominant role in the stress change (Figure 5). We do not use the first earthquake (1498 Meio) as a reference, as in the calculation in Figure 8. Thus we use interplate earthquakes of 1605, 1707, 1854, and 1944 as a reference. In Figures 9a and 9b, we do not include inland earthquakes as deformation sources. For comparison, we consider the inland earthquakes listed in Table 3 to be deformation sources in Figures 9c and 9d. Figures 9a and 9c employ the SP model and Figures 9b and 9d employ the TP model.

A number of disastrous inland earthquakes have occurred in the region (Table 4) [*National Astronomical Observatory*, 2011], although the magnitudes of some earthquakes have not been determined. Using the same procedure used to depict the superimposed and normalized $\Delta CFF_i(t)$ in Figure 8, we superimposed the activity of the inland earthquakes relative to the occurrence times of interplate earthquakes. The result is shown by histograms in Figure 9 (right axis). Here it should be noted that all the inland earthquakes after the 887 Ninna earthquake are superimposed to increase the number of inland earthquakes counted in Figure 9. The reverse and strike-slip earthquakes in Table 3, which occurred within the region surrounded by the thick dotted line in Figure 3, are indicated by dark gray and white bars, respectively, whereas light gray bars show earthquakes that are not listed in Table 3 but are listed in Table 4. If both a strike-slip fault and a reverse fault ruptured during the same earthquake, as happened in the 1586 and 1662 earthquakes, half of a point is assigned to each mechanism.

From the histograms in Figure 9, we can see the increase in activity in the period from 50 years before to 20 years after the occurrence of the interplate earthquakes. This has been pointed out in previous studies [*Utsu*, 1974; *Hori and Oike*, 1996]. It should be noted that all the known reverse fault movements occurred before the interplate earthquakes, although the mechanisms for most inland earthquakes are not known. On the other hand, strike-slip movements are known to have occurred in the periods both before and after interplate earthquakes.

On the basis of the temporal changes in the superimposed and normalized increment value profiles for all the faults (dotted purple and solid black lines), it is clear that the increment values gradually increase before an interplate earthquake, reach the largest soon after the earthquake, and then quickly decrease. Consistency of the increment values with the histograms of disastrous earthquakes in Figure 9c and 9d, where the inland earthquakes are used as the deformation sources, becomes better than that in Figure 9a and 9b, indicating the importance of interaction between inland earthquakes. Comparing $\Delta\mathrm{CFF}(t)$ (dotted brown line) and $\Delta\tau_s(t)$ (solid black line), the latter is more consistent with the historical record. This result suggests that apparent coefficient of friction μ' is lower than 0.3, which agrees with the result presented in section 3.3.

On the other hand, the superimposed and normalized increment value profiles for the reverse faults (dotted orange and solid red lines) are highest before the interplate earthquake and sharply decrease thereafter. This is consistent with the historical records, although the number of documented reverse fault earthquakes is small. The increment value profiles for strike-slip faults (dotted light blue and solid deep blue lines) show that the values before the earthquake are consistently small, hit a large peak just after the interplate earthquake, and quickly decrease.

The superimposed and normalized increment value profiles differ depending on whether inland earthquakes are considered as deformation sources. This dissimilarity reflects the fact that inland earthquakes generally enhance other faulting. The increment value profiles are basically consistent with the historical records if inland earthquakes are considered as the deformation sources. The difference in the increment value profiles between SP and TP models is generally small, mainly because the slip amounts of 1605 Keicho and 1944/1946 Showa events are similar for both models (Table 2). However, even if we elongate the computation period of the increment value profiles, both models give very similar results.

5. Discussion

As discussed above, focal mechanisms of inland earthquakes correspond to the fault mechanisms in and around the Kinki region, as a reflection of the local stress fields [e.g., *Townend and Zoback*, 2006; *Terakawa and Matsu'ura*, 2010; *Yukutake et al.*, 2012]. That is, reverse earthquakes occur in the northwestern and southwestern Chubu and central Kinki regions and strike-slip earthquakes occur in the western Chubu and northwestern Kinki regions. This corresponds to the fault mechanisms shown in Figure 3. Conversely, focal mechanisms for inland earthquakes in this region can be roughly inferred from the fault mechanisms. Our results predict that inland reverse faulting increases before the interplate earthquakes along the Nankai Trough, whereas strike-slip faulting increases after the interplate earthquakes. On the basis of this prediction, we can expect that inland earthquakes increase in the reverse fault region before interplate earthquakes, whereas inland earthquakes increase in the strike-slip fault region after interplate earthquakes. Figure 10 shows the spatiotemporal pattern of inland earthquakes whose epicentral coordinates are identified, as shown in Table 4. The expected correlation is notably consistent with the earthquake occurrences in the reverse fault region (central Kinki and southwestern Chubu regions), except for earthquakes A (in 1510) and B (in 1945) in Figure 10b. However, we note that earthquake B occurred after the 1944 Tonankai earthquake and elastic changes due to the Tonankai earthquake are positive on reverse faults around earthquake B (Figure 5e). This is consistent with the occurrence of earthquake B. On the other hand, in the strike-slip fault region, the expected correlation is consistent with earthquakes in the western Chubu region (earthquake occurrence rate increases after interplate earthquakes), but not consistent in the northwestern Kinki region (occurrence rate increases before interplate earthquakes). However, on the strike-slip faults, the highest value of ΔCFF(t) is updated most of the time and the elastic stress changes due to interplate earthquakes are relatively small in the northwestern Kinki region (e.g., fault m in Figure 7). As a whole, our result of inland earthquake occurrences is supported by the spatiotemporal pattern of inland earthquakes based on historical records, especially the pattern in the reverse faulting region.

As described above, this study predicts that inland reverse faulting increases before the occurrence of interplate earthquakes along the Nankai Trough, whereas strike-slip faulting increases after that. Recently, a similar relation has been observed in the seismic records collected before and after the 2011 great Tohoku-oki earthquake [e.g., *Asano et al.*, 2011; *Yoshida et al.*, 2012]. In the northern Tohoku region, the focal mechanisms of inland faults show an increased tendency for strike-slip mechanisms (minimum principal stress is horizontal in the NW–SE direction), as contrasted with reverse mechanisms (minimum principal stress is vertical) before the great earthquake.

Yoshida et al. [2012] explained that the E-W compression mainly generates inland reverse faulting in this region, and the 2011 great Tohoku-oki interplate earthquake dragged the northern Tohoku region toward the SE. Thus, strike-slip earthquakes occurred. The northern Tohoku region and the Kinki region are similar in that the long-term E-W compression generates inland earthquakes and interplate earthquakes drag the regions toward the SSE. On the other hand, the two regions differ in that in the Kinki region, about half of inland active faults are strike-slip suggesting that the minimum principal stress ranges from horizontal to vertical in the basic stress field [*Tsutsumi et al*., 2012], and the mechanisms of inland earthquakes are more sensitive to the stress change. In contrast, the elastic stress change due to interplate earthquakes is larger in the northern Tohoku region (0.5–1.0 MPa for the 2011 earthquake) than that in the central Kinki region (0.1–0.3 MPa for the interplate earthquakes along the Nankai Trough), which explains why the change in mechanism occurred in the Tohoku region.

In comparison with previous findings regarding viscoelastic stress change on inland active faults in and around the Kinki region, our present study results show faster viscous relaxation. This is because the previous models used larger viscosities and have lower end of viscoelastic medium, which results in the increase of relaxation time of slip response function in the model. Our rheological model consists of an elastic layer (thickness H = 35 km) overlying the viscoelastic half-space (viscosity $\eta = 5 \times 10^{18}$ Pa s). On the other hand, the rheological model of *Pollitz and Sacks* [1997] consists of an elastic layer (H = 22 km) over a viscoelastic lower layer ($\eta = 8 \times 10^{18}$ Pa s, thickness = 19 km) on the elastic half-space. The rheological model of *Hyodo and Hirahara* [2004] and *Hirahara et al*. [2006] consists of an elastic layer (H = 30 km) overlying a viscoelastic layer ($\eta = 1.0 \times 10^{19}$ Pa s).

Among the previous works, *Hyodo and Hirahara* [2004] calculated ΔCFF in a similar situation to the present study. However, the stress accumulation rate in Figure 9 of their paper is slower than that of Figure 7 of the present study. What causes this difference? In their setting, NKTZ strain rate is fully consumed by inland earthquakes, and thus its rate (1.0×10^{-7} year^{-1}) is around three times as fast as that of the present study. On the other hand, the calculated stress accumulation rate in Figure 9 of their paper is around 1/10 of their setting, which would be their mistake. As a result, the stress accumulation rate in Figure 9 of their paper is around 1/3 of Figure 7 of the present study.

We estimated the strain consumption rate due to inland earthquakes from inland faults with surface rupture. However, considering the existence of some inland earthquakes with blind faults even in large earthquakes, the actual values are possibly larger. If we use a larger strain and stress accumulation on inland faults, the increment values soon after interplate earthquakes decrease. It is really difficult to estimate the values of strain and stress accumulation on inland faults. However, under the larger values (e.g., $\Delta\varepsilon_{\mathrm{NKTZ}} = 0.4 \times 10^{-7}$ year^{-1}, or $\Delta\sigma_{\mathrm{NKTZ}} = 4$ kPa/year from equation (4)), we can obtain a similar temporal pattern and decrease the increment values soon after interplate earthquakes, as shown in Figure 11.

In this study, we show that the degree to which the highest value of ΔCFF(t) on a fault is renewed during a certain period can be related to the potential of earthquake occurrence on that fault. However, *Freed* [2005] reviewed the processes that delay the occurrence of earthquakes after elastic stress changes, such as afterslip from the interplate earthquakes, viscoelastic relaxation in the lower crust, and decreases in fault friction related to rate- and state-dependent laws, which are not considered in this study.

For a more detailed estimation of stress changes, further studies should focus on (1) detailed stress accumulation pattern on inland faults due to the NKTZ compression, (2) the finite element modeling with detailed crustal structure, (3) the detailed spatiotemporal slip distribution of interplate earthquakes, (4) the detailed geometry of inland faults, and (5) the mechanism of inland earthquakes.

6. Conclusions

We investigated the mechanical relationship between interplate and inland earthquakes in and around the Kinki region using long-term changes in CFF on inland faults. In the computation of ΔCFF on inland earthquakes, we incorporated the east-west compression known as the Niigata–Kobe Tectonic Zone (NKTZ), historical great interplate earthquakes along the Nankai Trough, interseismic plate locking, and historical inland earthquakes as deformation sources.

The calculated long-term ΔCFF due to NKTZ east-west compression explains long-term stress accumulation on most faults in this region, which shows that the general strike trend of inland active faults in this region are determined by NKTZ compression and follow the standard theory of fault mechanics. Elastic ΔCFF or $\Delta\tau_s$ values due to interplate great earthquakes are negative for reverse faults near the Nankai Trough. At the same time, ΔCFF values are positive on strike-slip faults located NNW of the source region. This is caused by the general strike trend of the inland faults and by the direction the crust is dragged (to the SSE) due to the interplate earthquakes along the Nankai Trough. The amount of ΔCFF on inland faults in this region due to interplate earthquakes decreases northward as a function of distance from the source region, the Nankai Trough. Finally, we calculated the ΔCFF(t) on faults in this region due to all deformation sources: NKTZ compression, interplate locking, interplate earthquakes, and inland earthquakes. The calculated ΔCFF(t) are mostly consistent with the inland earthquake occurrences indicated by historical records even including disastrous historical earthquakes where there is no information on their source faults. If we use the change in shear stress instead of the change in CFF, the consistency is clearly enhanced, suggesting that the value of apparent coefficient of friction is low in this region. This study predicts that inland reverse faulting will increase before interplate earthquakes along the Nankai Trough and that strike-slip faulting will increase after interplate earthquakes occur. This prediction is supported by the spatiotemporal pattern of inland earthquakes from historical records, if we assume that fault mechanisms in this region represent the focal mechanisms.

Acknowledgments

We thank Norio Shigematsu for his useful comments. We also acknowledge the comments by Robert Nowack, an anonymous associate editor and anonymous reviewers in improving the manuscript. This study has been financially supported by the MEXT projects “New Research Project for the Evaluation of Seismic Linkage around the Nankai Trough” and “Observation and Research Program for Prediction of Earthquakes and Volcanic Eruptions.” We used the supercomputer of ACCMS, Kyoto University, and ITC, University of Tokyo. Figures were plotted using the GMT software [*Wessel and Smith*, 1998].

References

Anderson, E. M. (1951), *The dynamics of faulting*, Oliver and Boyd, Edinburgh.

Asano, Y., T. Saito, Y. Ito, K. Shiomi, H. Hirose, T. Matsumoto, S. Aoi, S. Hori, and S. Sekiguchi (2011), Spatial distribution and focal mechanisms of aftershocks of the 2011 off the Pacific Coast of Tohoku Earthquake, *Earth*, *Planets Space*, *63*(7), 669–673, doi:10.5047/eps.2011.06.016.

Bird, P. (2003), An updated digital model of plate boundaries, *Geochem*. *Geophys*. *Geosyst*., *4*, 1027, doi:10.1029/2001GC000252.

DeMets, C., R. G. Gordon, D. F. Argus, and S. Stein (1994), Effect of recent revisions to the geomagnetic reversal time scale on estimates of current plate motions, *Geophys*. *Res*. *Lett*., *21*(20), 2191–2194, doi:10.1029/94GL02118.

Earthquake Research Committee (2001), Long-term evaluation of earthquakes along the Nankai Trough, http://www.jishin.go.jp/main/chousa/kaikou_pdf/nankai.pdf. (in Japanese).

Earthquake Research Committee (2005), Supplement of Report: 'Methods of evaluating active fault for fundamental survey and observation', http://www.jishin.go.jp/main/choukihyoka/05aug_hyokashuhou/furoku.pdf. (in Japanese).

Freed, A. M. (2005), Earthquake triggering by static, dynamic and postseismic stress transfer, *Annu*. *Rev*. *Earth* *Planet*. *Sci*., *33*, 335–367, doi:10.1146/annurev.earth.33.092203.122505.

Fukahata, Y. and M. Matsu'ura (2006), Quasi-static internal deformation due to a dislocation source in a multilayered elastic/viscoelastic half-space and an equivalence theorem, *Geophys. J. Int.*, *166*(1), 418–434, doi:10.1111/j.1365-246X.2006.02921.x.

Harris, R. A. (1998), Introduction to Special Section: Stress Triggers, Stress Shadows, and Implications for Seismic Hazard, *J. Geophys. Res.*, *103*(B10), 24347–24358, doi:10.1029/98JB01576.

Hashimoto, C., K. Fukui, and M. Matsu'ura (2004), 3-D modelling of plate interfaces and numerical simulation of long-term crustal deformation in and around Japan, *Pure Appl. Geophys.*, *161*(9–10), 2053–2068, doi:10.1007/s00024-004-2548-8.

Heki, K., and S. Miyazaki (2001), Plate convergence and long-term crustal deformation in central Japan, *Geophys. Res. Lett.*, *28*(12), 2313–2316, doi:10.1029/2000GL012537.

Hirahara, K., T. Hori, M. Hyodo, and N. Mitsui (2006), Generation cycle of great earthquakes along the Nankai trough and the occurrence of inland earthquakes in southwestern Japan, Abstr. Seismol. Soc. Jpn., 2006 Fall Meeting, 21 (in Japanese).

Hori, T., and K. Oike (1996), A Statistical Model of Temporal Variation of Seismicity in the Inner Zone of Southwest Japan Related to the Great Interplate Earthquakes along the Nankai Trough, *J. Phys. Earth*, *44*, 349–356.

Hori, T., and K. Oike (1999), A Physical Mechanism for Temporal Variation in Seismicity in the Inner Zone of Southwest Japan Related to the Great Interplate Earthquakes along the Nankai Trough, *Tectonophysics*, *308*(1–2), 83–98, doi:10.1016/S0040-1951(99)00079-7.

Hyodo, M., and K. Hirahara (2003), A viscoelastic model of interseismic strain accumulation in Niigata-Kobe Tectonic Zone of central Japan, *Earth, Planets Space*, *55*, 667–675.

Hyodo, M., and K. Hirahara (2004), GeoFEM kinematic earthquake cycle simulation in southwest Japan, *Pure Appl. Geophys.*, *161*(9–10), 2069–2090, doi:10.1007/s00024-004-2549-7.

Iio, Y. (1997), Frictional coefficient on faults in a seismogenic region inferred from earthquake mechanism solutions, *J. Geophys. Res.*, *102*(B3), 5403–5412, doi:10.1029/96JB03593.

Iio, Y., T. Sagiya, Y. Kobayashi, and I. Shiozaki (2002), Water-weakened lower crust and its role in the concentrated deformation in the Japanese Islands, *Earth Planet. Sci. Lett.*, *203*(1), 245–253, doi:10.1016/S0012-821X(02)00879-8.

Ishibashi, K. (1976), Re-examination of a great earthquake expected in the Tokai district: possibility of the "Suruga Bay earthquake", Abstr. Seismol. Soc. Jpn., 1976(2), 30–34 (in Japanese).

Ishibashi, K. (2004), Status of historical seismology in Japan, *Ann. Geophys.*, *47*(2–3), 339–368.

Kaizuka, S., and T. Imaizumi, (1984), Horizontal Strain Rates of the Japanese Islands Estimated from Quaternary fault data, *Geogr. Rep. Tokyo Metrop. Univ.*, *19*, 43–65.

Kreemer, C., W. E., Holt, and A. J. Haines (2003). An integrated global model of present-day plate motions and plate boundary deformation, *Geophys. J. Int.*, *154*(1), 8–34, doi:10.1046/j.1365-246X.2003.01917.x.

Mazzotti, S., X. Le Pichon, P. Henry, and S.-I. Miyazaki (2000), Full interseismic locking of the Nankai and Japan-west Kurile subduction zones: An analysis of uniform elastic strain accumulation in Japan constrained by permanent GPS, *J. Geophys. Res.*, *105*(B6), 13159–13177, doi:10.1029/2000JB900060.

Mikumo, T., and M. Ando, (1976), A search into the faulting mechanism of the 1891

great Nobi earthquake, *J. Phys. Earth*, *24*, 63–87.
Miyazaki, S., and K. Heki (2001), Crustal velocity field of southwest Japan: Subduction and arc-arc collision, *J. Geophys. Res.*, *106*(B3), 4305–4326, doi:10.1029/2000JB900312.
National Astronomical Observatory (2011), *Rika Nenpyo 2012 (Chronological Scientific Tables)*, Maruzen, Tokyo (in Japanese).
Oppenheimer, D. H., P. A. Reasenberg, and R. W. Simpson (1988), Fault plane solutions for the 1984 Morgan Hill, California, Earthquake Sequence: Evidence for the state of stress on the Calaveras Fault, *J. Geophys. Res.*, *93*(B8), 9007–9026, doi:10.1029/JB093iB08p09007.
Pollitz F. F., and S. Sacks (1997), The Kobe, Japan, Earthquake: A Long-Delayed Aftershock of the Offshore 1944 Tonankai and 1946 Nankaido Earthquakes, *Bull. Seismol. Soc. Am.*, *87*(1), 1–10.
Reasenberg, P. A., and R. W. Simpson (1992), Response of regional seismicity to the static stress change produced by the Loma Prieta earthquake, *Science*, *255*, 1687–1690.
Sagiya, T. (2004), A decade of GEONET: 1994-2003 - The continuous GPS observation in Japan and its impact on earthquake studies -, *Earth, Planets Space, 56,* xxix-xli.
Sagiya, T., S. Miyazaki, and T. Tada (2000), Continuous GPS Array and Present-day Crustal Deformation of Japan, *Pure Appl. Geophys.*, *157*(11–12), 2303–2322, doi:10.1007/PL00022507.
Sato, H. (1973), A study of horizontal movement of earth crust associated with destructive earthquakes in Japan, *Bull. Geogr. Surv. Inst.*, *19*, 89–130.
Sato, T., and M. Matsu'ura, (1993), A kinematic model for evolution of island arc-trench

systems, *Geophys. J. Int.*, *114*(3), 512–530. doi:10.1111/j.1365-246X.1993.tb06984.x.

Savage, J. C. (1983), A dislocation model of strain accumulation and release at a subduction zone, *J. Geophys. Res.*, *88*(B6), 4984–4996, doi:10.1029/JB088iB06p04984.

Sella, G. F., T. H. Dixon, and A. Mao (2002), REVEL: A model for Recent plate velocities from space geodesy, *J. Geophys. Res.*, *107*(B4), 2081, doi:10.1029/2000JB000033.

Shimazaki, K., and T. Nakata (1980), Time-predictable recurrence model for large earthquakes, *Geophys. Res. Lett.*, *7*(4), 279–282, doi:10.1029/GL007i004p00279.

Terakawa, T., and M. Matsu'ura (2010), The 3-D tectonic stress fields in and around Japan inverted from centroid moment tensor data of seismic events, *Tectonics*, *29*, TC6008, doi:10.1029/2009TC002626.

Townend, J., and M. D. Zoback (2006), Stress, strain, and mountain building in central Japan, *J. Geophys. Res.*, *111*, B03411, doi:10.1029/2005JB003759.

Tsutsumi, H., K. Sato, and A. Yamaji (2012), Stability of the regional stress field in central Japan during the late Quaternary inferred from the stress inversion of the active fault data, *Geophys. Res. Lett.*, *39*, L23303, doi:10.1029/2012GL054094.

Utsu, T. (1974), Correlation between Great Earthquakes along the Nankai Trough and Destructive Earthquakes in Western Japan, Rep. Cood. Comm. Eartq. Predict., *12*, 120–122 (in Japanese).

Wessel, P., and W. H. F. Smith (1998), New, improved version of Generic Mapping Tool released, *EOS, Trans., Amer. Geophys. Union*, *79*, 579.

Yoshida, K., A. Hasegawa, T. Okada, T. Iinuma, Y. Ito, and Y. Asano (2012), Stress before and after the 2011 great Tohoku-oki earthquake and induced earthquakes in inland areas of eastern Japan, *Geophys*. *Res*. *Lett*., *39*, L03302, doi:10.1029/2011GL049729.

Yukutake, Y., T. Takeda, and A.Yoshida (2012), Focal mechanism determination of intraplate earthquakes, by using the absolute amplitude of body waves, Abstr. Seismol. Soc. Jpn., 2006 Fall Meeting, 238 (in Japanese).

Table 1. Locations, Surface Geometry, and Fault Type, Inland Active Faults shown in Figure 3[a]

Fault Name	T.	Lat. (°N)	Lon. (°E)	Str. (°)	Len. (km)	Fault Name	T.	Lat. (°N)	Lon. (°E)	Str. (°)	Len. (km)	Fault Name	T.	Lat. (°N)	Lon. (°E)	Str. (°)	Len. (km)
Atotsugawa$_i$	R	35.56	137.59	60	69	Neodani$_k$	L	35.64	136.60	325	30	Yamada	R	35.58	135.09	50	33
Kokufu	R	36.13	137.12	50	27	Umehara$_l$	L	35.53	136.81	305	36	Gomura$_m$	L	35.72	134.99	330	34
Takayama	R	36.01	137.20	50	48	Mitahora	L	35.48	136.78	300	19	Nara Plain E	T	34.68	135.83	350	35
Inohana	R	35.99	137.39	60	24	Ibigawa	L	35.71	136.48	300	24	Arima$_e$	R	34.85	135.38	80	55
Ushikubi	R	36.42	137.13	50	54	Mugigawa	L	35.59	136.48	300	29	Ikoma	T	34.70	135.65	10	38
Shogawa	L	36.20	136.93	340	67	Yanagase NN	T	36.00	136.00	20	24	Kanbayashi	R	35.35	135.38	60	26
Atera N	L	36.22	137.20	350	17	Yanagase NS	T	35.83	136.04	320	24	Mitoke	L	35.24	135.33	290	26
Atera S$_c$	L	35.68	137.35	310	60	Yanagase M	L	35.69	136.16	350	12	NishiyamaN	L	35.10	135.52	300	21
Sami	R	35.67	137.23	60	25	Yanagase S	L	35.49	136.34	310	45	NishiyamaS	T	34.96	135.66	180	21
Shirakawa	R	35.63	137.23	65	31	Urazoko	L	35.67	136.10	310	25	Rokko S	R	34.73	135.30	60	50
Byobuyama	T	35.47	137.51	60	15	Nosaka	L	35.70	135.93	319	31	Awaji W$_o$	R	34.58	134.98	60	23
Ako	T	35.51	137.30	310	23	Shufukuji	L	35.57	136.13	320	10	Awaji E	R	34.53	134.98	50	25
Enasan E	T	35.36	137.38	55	37	KohokuR NW	R	35.58	136.05	30	25	Senzan	T	34.38	134.85	210	12
Enasan W	R	35.25	137.19	45	22	KohokuR SE	R	35.53	136.06	40	16	Uemachi	T	34.63	135.45	10	42
Sanage-Taka N	T	35.13	137.08	220	35	Biwako W N	T	35.38	136.03	180	23	Kongo R E	T	34.46	135.69	180	17
Sanage-Taka S	T	34.93	137.01	335	16	Biwako W S$_b$	T	35.13	135.98	200	38	Izumi R S$_{III}$	R	34.32	135.38	250	48
Kagiya N	T	34.99	136.93	165	13	Yoro N$_d$	T	35.22	136.60	158	30	Kitan$_{II}$	R	34.21	134.89	250	47
Kagiya S	T	34.85	136.89	350	26	Yoro S	T	34.98	136.64	203	30	Sanuki R S$_I$	R	34.03	133.96	250	130
Ochigata	T	36.87	136.86	35	44	Suzuka E	T	35.13	136.45	190	35	Nagisen	R	35.13	134.06	80	32
Tonami W	T	36.63	136.86	220	26	Suzuka W	T	35.12	136.34	0	44	YamasakiW$_a$	L	35.01	134.49	300	51
Tonami E	T	36.56	136.95	30	21	Tongu	T	34.83	136.21	0	31	YamasakiE	L	34.88	134.88	310	30
Kurehayama	T	36.68	137.20	210	22	Nunobiki E W	T	34.77	136.43	170	33	Kusatani	R	34.76	134.94	60	13
Morimoto	T	36.57	136.68	23	26	Nunobiki E E	T	34.66	136.54	200	48	Nagao	T	34.23	134.13	80	24
FukuiP E E$_\alpha$	L	36.23	136.29	0	45	Kizugawa$_h$	T	34.80	136.10	250	31	Ise Bay N	T	34.87	136.78	340	25
FukuiP E W$_n$	L	36.16	136.21	340	33	Mikata$_f$	T	35.57	135.89	0	26	Shiroko	T	34.77	136.69	270	21
Nagaragawa	L	35.83	136.89	330	29	Hanaore N$_{g\beta}$	R	35.30	135.91	20	26	Osaka Bay	T	34.53	135.14	205	39
Nukumi NW$_j$	L	35.85	136.42	320	16	Hanaore M$_\gamma$	R	35.10	135.83	20	20	Uozu	T	36.80	137.47	30	32
Nukumi SE	L	35.76	136.58	300	21	Hanaore S	T	34.96	135.81	0	15						

[a]Abbreviations for headings: T., fault type; Lat., Latitude; Lon., Longitude; Str., Strike measured clockwise from the north; Len., Length. Abbreviations for fault types: L, Left-lateral strike-slip; R, Right-lateral strike-slip; T, Reverse fault (Thrust). Latitude and longitude show the midpoint of surface rupture of the fault. Subscripts at fault names correspond to faults in Figure 3 (alphabet and Roman number) and Figure 4a (Greek alphabet). Locations, surface geometry, and fault type are from the *Earthquake Research Committee* [2005].

Table 2. Spatiotemporal Distribution, Amount of Calculated Slip for Interplate Earthquakes, Nankai Trough[a]

	Region					Region				
	A	B	C	D	E	A	B	C	D	E
Relative motion s_{rate} (cm/yr)	6.5	6.0	4.5	3.5	2.0	6.5	6.0	4.5	3.5	2.0
Date: Name	Slip by SP model (m)					Slip by TP model (m)				
29 Nov 0684: Tenmu	?	?	-	-	-	13.2	12.2	-	-	-
26 Aug 0887: Ninna	13.2	12.2	?	?	-	13.7	12.7	9.4	7.3	-
17 Dec 1096: Eicho-Tokai	-	-	9.4	7.3	?	-	-	11.9	9.2	8.0
22 Feb 1099: Kowa-Nankai	13.7	12.7	-	-	-	17.1	15.7	-	-	-
22 Nov 1360: Shohei-Tonankai	-	-	11.9	9.2	-	-	-	6.2	4.8	-
03 Aug 1361: Shohei-Nankai	17.1	15.7	-	-	-	8.9	8.2	-	-	-
09 Jul 1498: Meio-Nankai	8.9	8.2	-	-	-	6.9	6.4	-	-	-
20 Sep 1498: Meio-Tokai	-	-	6.2	4.8	8.0	-	-	4.8	3.7	4.2
03 Feb 1605: Keicho	6.9	6.4	4.8	3.7	-	6.7	6.2	4.6	3.6	-
28 Oct 1707: Hoei	6.7	6.2	4.6	3.6	4.2	9.6	8.8	6.6	5.2	2.9
23 Dec 1854: Ansei-Tokai	-	-	6.6	5.2	2.9	-	-	4.0	3.1	3.7
24 Dec 1854: Ansei-Nankai	9.6	8.8	-	-	-	6.0	5.5	-	-	-
07 Dec 1944: Showa-Tonankai	-	-	4.0	3.1	-	-	-	4.2	3.3	-
21 Dec 1946: Showa-Nankai	6.0	5.5	-	-	-	6.0	5.5	-	-	-
(18 Dec 2038: Heisei)	(6.0)	(5.5)	(4.2)	(3.3)	(3.7)	?	?	?	?	?

[a]Date = earthquake occurrence date (after *National Astronomical Observatory* [2011]) by the Gregorian calendar. SP = slip predictable model, TP = time predictable model. Question marks = areas where the slip amount cannot be determined by the prediction models. Hyphens = areas without certain or probable historical record of earthquake occurrence.

Table 3. Source Faults for Historically Recorded Earthquakes, Inland Active Faults, Kinki Region[a]

No.	Date	Fault Name	Lat. (°N)	Lon. (°E)	Strike (°)	Dip (°)	Rake (°)	Length (km)	Slip (m)
a	03 Aug 0868$_1$	Yamasaki NW	35.01	134.49	300	90	0	51	2
b	13 Aug 1185$_2$	Biwako W Coast S	35.16	135.85	200	40	90	38	4
c	18 Jan 1586$_3$	Atera S	35.68	137.35	310	90	0	60	4.5
d		Yoro Kuwana N	35.22	136.60	157.5	40	90	32	8
e	05 Sep 1596$_4$	Arima Takatsuki	34.85	135.38	260	90	180	55	3
f	16 Jun 1662$_5$	Mikata	35.57	135.89	0	40	90	26	4
g		Hanaore N	35.30	135.91	20	90	180	26	3.5
h	09 Jul 1854$_6$	Kizugawa	34.80	136.10	250	40	90	31	2.5
i	09 Apr 1858$_7$	Atotsugawa	36.43	137.27	60	90	180	69	6.3
j	28 Oct 1891$_8$	Nukumi NW	35.85	136.43	320	90	0	16	1
k		Neodani	35.64	136.60	325	90	0	30	2.5
l		Umehara	35.53	136.81	305	90	0	36	3
m	07 Mar 1927$_9$	Gomura	35.72	134.99	330	90	0	34	3
n	28 Jun 1948$_{10}$	Fukui Plain East W	36.16	136.21	340	90	0	33	2
o	17 Jan 1995$_{11}$	Awaji West Coast	34.58	134.98	60	90	180	23	2.5

[a]Identified faults are from the *Earthquake Research Committee* [2005]. Date = earthquake occurrence date (after *National Astronomical Observatory* [2011]) by the Gregorian calendar. Subscript numbers in the “Date” column correspond to earthquakes in Table 4. Latitude and longitude show the midpoint of surface rupture of the fault. Strike is measured clockwise from the north, rake is measured on the fault surface counterclockwise from strike. Fault numbers are the same as Figure 3.

Table 4. Disastrous Inland Earthquakes from the year 827 to 1969[a]

Date	Magnitude M	Location		Date	Magnitude M	Location		Date	Magnitude M	Location	
		Lat. (°N)	Lon. (°E)			Lat. (°N)	Lon. (°E)			Lat. (°N)	Lon. (°E)
11 Aug 0827	6.5–7.0	35.0	135.75	13 May 1449	5.75–6.5	35.0	135.75	19 Aug 1830	6.5	35.1	135.6
?? ??? 0856	6–6.5	around	Kyoto	29 May 1466	?	around	Kyoto	27 May 1833	≈6.25	35.5	136.6
03 Aug 0868$_{1}$	≥7.0	34.8	134.8	19 Jun 1494	≈6.0	34.6	135.7	09 Jul 1854$_{6}$	7.25	34.75	136.1
13 Jan 0881	6.4	around	Kyoto	21 Sep 1510$_{A}$	6.5–7.0	34.6	135.6	18 Mar 1855	6.75	36.25	136.9
10 Jul 0890	≈6.0	around	Kyoto	25 Feb 1579	6.0	34.7	135.5	09 Apr 1858$_{7}$	7.0–7.1	36.4	137.2
16 Jul 0934	≈6.0	around	Kyoto	18 Jan 1586$_{3}$	≈7.8	36.0	136.9	09 Apr 1858	?	North.	Kinki
22 May 0938	≈7.0	35.0	135.8	05 Sep 1596$_{4}$	7.5	34.65	135.6	24 Feb 1865	≈6.25	Western	Kinki
22 Jul 0976	≥6.7	34.9	135.8	23 Nov 1640	6.25–6.75	36.3	136.2	28 Oct 1891$_{8}$	8.0	35.6	136.6
?? ??? 1038	?	34.3	135.6	16 Jun 1662$_{5}$	7.25–7.6	35.2	135.95	22 Mar 1900	5.8	35.8	136.2
25 Aug 1041	?	around	Kyoto	04 Jan 1664	5.9	around	Kyoto	14 Aug 1909	6.8	35.4	136.3
01 Dec 1070	6.0–6.5	34.8	135.8	25 Jun 1665	≈6.0	around	Kyoto	26 Nov 1916	6.1	34.6	135.0
28 Sep 1091	6.2–6.5	34.7	135.8	?? ??? 1685	?	SW	Chubu	23 May 1925	6.8	35.6	134.8
19 Mar 1093	6.0–6.3	around	Kyoto	12 Dec 1694	?	North.	Kinki	07 Mar 1927$_{9}$	7.3	35.6	134.9
26 Nov 1177	6.0–6.5	34.7	135.8	02 Feb 1715	6.5–7	35.4	136.6	17 Oct 1930	6.3	36.4	136.3
13 Aug 1185$_{2}$	≈7.4	35.0	135.8	17 Jun 1725	≈6.0	36.4	136.4	21 Feb 1936	6.4	34.5	135.7
27 Aug 1245	?	around	Kyoto	13 Nov 1731	?	Central	Kinki	13 Jan 1945$_{B}$	6.8	34.7	137.1
24 Feb 1317	6.5–7.0	35.0	135.8	26 Mar 1751	5.5–6	35.0	135.8	28 Jun 1948$_{10}$	7.1	36.2	136.3
05 Dec 1325	6.5	35.6	136.1	18 Nov 1802	6.5–7	35.2	136.5	07 Mar 1952	6.5	36.5	136.1
06 Jul 1350	≈6.0	35.0	135.8	01 Mar 1815	≈6.0	36.4	136.5	19 Aug 1961	7.0	36.1	136.7
01 Aug 1361	?	around	Kyoto	02 Aug 1819	7.25	35.2	136.3	27 Mar 1963	6.9	35.8	135.8
23 Dec 1425	≈6.0	35.0	135.8	28 Aug 1826	≈6.0	36.2	137.25	09 Sep 1969	6.6	35.8	137.1

[a]Disastrous earthquakes occurred in the region surrounded by thick dotted line in Figure 3 from 80 years before the 887 Ninna event to 40 years after the 1944 Showa Tonankai earthquake. Data are from *National Astronomical Observatory* [2011], and date is by the Gregorian calendar. Subscript numbers correspond to earthquakes in Table 3 and Figure 10.

Figure Captions

Figure 1. Tectonic setting in central Japan. Thick solid lines represent plate boundaries after *Bird* [2003]. Abbreviations for plates: NAM, North American; OKH, Okhotsk; EUR, Eurasian; AMR, Amurian; PHS, Philippine Sea. Smooth thin solid lines are depth contours on the upper surface of the PHS plate [*Hashimoto et al*., 2004], contour interval 10 km. The thick dotted line represents the high strain rate zone called the Niigata–Kobe Tectonic Zone (NKTZ), after *Sagiya et al*. [2000]. The thick lines enclosed by the chain lines in the NKTZ denote the representative inland faults discussed in the text (names are boxed). Thin broken lines show the regional boundaries of Japan, and underlined words are region names. Gray areas are slip regions (A-E) of interplate earthquakes along the Nankai Trough [*Earthquake Research Committee*, 2001].

Figure 2. Spatiotemporal distribution of certain and probable great interplate earthquakes along the Nankai Trough as deduced from historical records [*Ishibashi*, 2004]. The top panel shows the source regions of interplate earthquakes [*Earthquake Research Committee*, 2001]. The location of the Nankai Trough is after *Bird* [2003]. Five arrows in regions A-E indicate convergence vectors between EUR and PHS, whose rates are after *Heki and Miyazaki* [2001]. Date is the earthquake occurrence date (after *National Astronomical Observatory* [2011]) by the Gregorian calendar.

Figure 3. Inland active faults in and around the Kinki region. Fault locations from the *Earthquake Research Committee* [2005]. Barbs indicate the hanging walls of reverse faults. Thick and thin lines indicate left-lateral and right-lateral strike-slip faults, respectively. Earthquakes on gray faults with lowercase letters are documented by historical records (Table 3). Faults with Roman numbers are right-lateral strike-slip

faults, part of the Median Tectonic Line. The thick dotted line outlines the region analyzed in Figure 9.

Figure 4. Long-term changes in CFF on inland active faults due to NKTZ east-west compression. Conditions defined for this model were uniform east-west compression with a direction of N100°E and a strain rate of 0.3×10^{-7} year^{-1}. (a) Changes in CFF with apparent coefficient of friction $\mu' = 0.3$. (b) Changes in shear stress, or changes in CFF with apparent coefficient of friction $\mu' = 0.0$. Greek letters correspond to subscript Greek letters in Table 1.

Figure 5. Coseismic changes in CFF on the inland active faults due to interplate earthquakes. The slip regions are (b) ABCDE, (c) ABCD, (d) AB, (e) CD, and (f) CDE, which correspond to the named earthquakes shown in Figure 2. The amount of slip in each region is set at the accumulated slip deficit for 100 years. For comparison, the changes in CFF for 100 years due to NKTZ compression are shown in (a) (the same figure as Figure 4a).

Figure 6. Time evolution of ΔCFF on (a) a reverse fault, “b” and (b) a strike-slip fault, “l” (Figure 3), due to the interplate earthquakes along the Nankai Trough and the following viscoelastic relaxation in the asthenosphere. The amount of slip given in the source regions at the interplate earthquakes is set to the slip deficit during 100 years.

Figure 7. ΔCFF(t) and $\Delta\tau_s(t)$ on the inland active faults with historically recorded earthquakes (Figure 3 and Table 3). ΔCFF(t) and $\Delta\tau_s(t)$ due to all the sources examined in this study (i.e., NKTZ compression, interplate earthquakes, interplate locking, and inland earthquakes) are shown by black and red lines, respectively. ΔCFF(t) and $\Delta\tau_s(t)$ due to only NKTZ compression are shown by light blue and orange lines, respectively. We also show the fault type. Abbreviations for fault types: L, Left-lateral strike-slip; R,

Right-lateral strike-slip; T, Reverse fault (Thrust).

Figure 8. Schematic diagram showing how superimposed and normalized $\Delta\mathrm{CFF}_i(t)$ was obtained. (a) Hypothetical $\Delta\mathrm{CFF}(t)$ on an idealized inland fault. Different gray levels show the number of years before or since the interplate earthquake along the Nankai Trough, from white (from −50 to −40 years) to dark gray (from −10 to 0 years) and from dark gray (from +0 to +10 years) to light gray (from +30 to +40 years). The thicknesses of bars projected to the left axis show "the increment values of the highest ΔCFF." (b) Temporal change in the increment values of the highest $\Delta\mathrm{CFF}(t)$, $\Delta\mathrm{CFF}_i(t)$. (c) Temporal change of $\Delta\mathrm{CFF}_i(t)$ which is superimposed and normalized. The horizontal axis represents time relative to the occurrence times of the great interplate earthquakes along the Nankai Trough.

Figure 9. Temporal distribution of the disastrous earthquakes (right axis) and the superimposed and normalized increment values (left axis), $\Delta\mathrm{CFF}_i(t)$ (dotted line) and $\Delta\tau_{si}(t)$ (solid line) on inland faults in the region surrounded by the thick dotted line in Figure 3. First, we obtain the superimposed and normalized increment value on each fault, as schematically presented in Figure 8. Then, the obtained values are averaged for examined faults (total number: 73; reverse faults: 29; strike-slip faults: 44). The histogram shows the number of disastrous earthquakes in Table 4. Dark gray and white bars show the reverse and strike-slip earthquakes in Table 3, respectively. The light gray bars show earthquakes not listed in Table 3, but listed in Table 4. The origin of the horizontal axis corresponds to the occurrence years of the Nankai Trough events in region CD.

Figure 10. Spatiotemporal distribution of inland earthquakes whose epicentral coordinates are given in Table 4. Thick dotted line shows the region analyzed. Circles of

different gray level and size show the relative time t_r to interplate earthquakes. “A” and “B” correspond to the two earthquakes with those letters shown as subscripts in the “Date” column in Table 4.

Figure 11. Same as Figure 9d, but under larger strain and stress accumulation rates on inland faults due to the NKTZ compression. Strain accumulation rates $\Delta\varepsilon_{\mathrm{NTKZ}}$ are (a) 0.4 $\times 10^{-7}$ year^{-1} and (b) 0.3 $\times 10^{-7}$ year^{-1}. Figure 11b is shown for comparison (the same figure as Figure 9d).

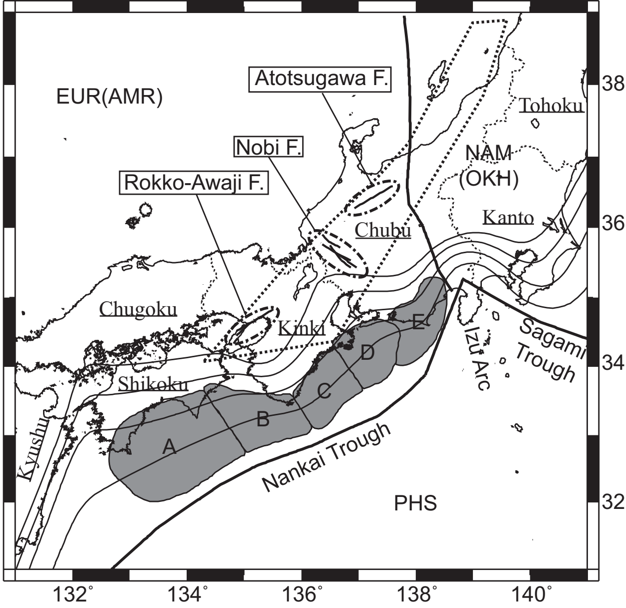

Figure 1. Tectonic setting in central Japan. Thick solid lines represent plate boundaries after *Bird* [2003]. Abbreviations for plates: NAM, North American; OKH, Okhotsk; EUR, Eurasian; AMR, Amurian; PHS, Philippine Sea. Smooth thin solid lines are depth contours on the upper surface of the PHS plate [*Hashimoto et al*., 2004], contour interval 10 km. The thick dotted line represents the high strain rate zone called the Niigata–Kobe Tectonic Zone (NKTZ), after *Sagiya et al*. [2000]. The thick lines enclosed by the chain lines in the NKTZ denote the representative inland faults discussed in the text (names are boxed). Thin broken lines show the regional boundaries of Japan, and underlined words are region names. Gray areas are slip regions (A-E) of interplate earthquakes along the Nankai Trough [*Earthquake Research Committee*, 2001].

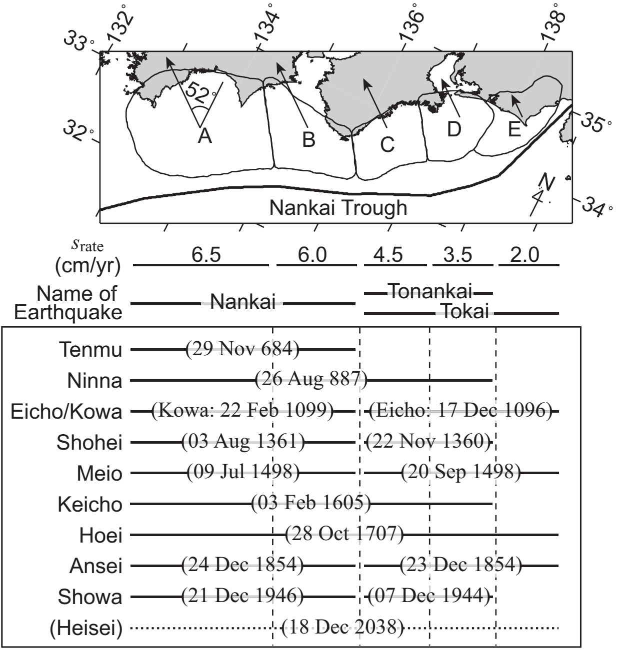

Figure 2. Spatiotemporal distribution of certain and probable great interplate earthquakes along the Nankai Trough as deduced from historical records [*Ishibashi*, 2004]. The top panel shows the source regions of interplate earthquakes [*Earthquake Research Committee*, 2001]. The location of the Nankai Trough is after *Bird* [2003]. Five arrows in regions A-E indicate convergence vectors between EUR and PHS, whose rates are after *Heki and Miyazaki* [2001]. Date is the earthquake occurrence date (after *National Astronomical Observatory* [2011]) by the Gregorian calendar.

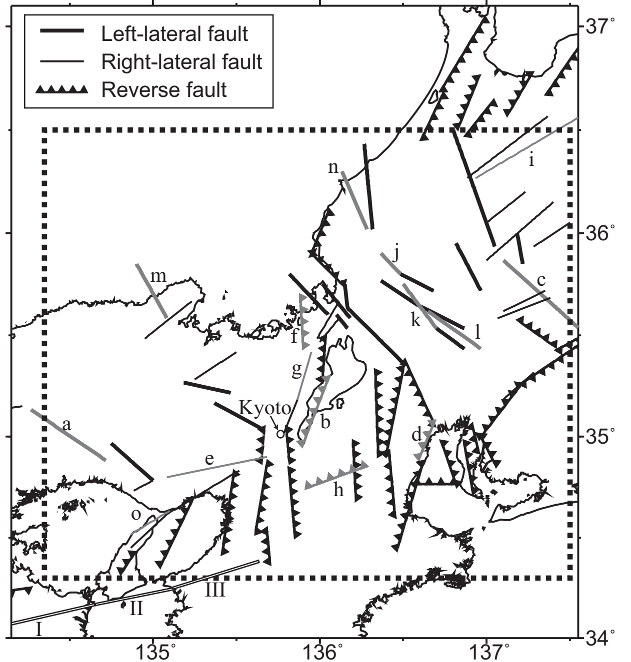

Figure 3. Inland active faults in and around the Kinki region. Fault locations from the *Earthquake Research Committee* [2005]. Barbs indicate the hanging walls of reverse faults. Thick and thin lines indicate left-lateral and right-lateral strike-slip faults, respectively. Earthquakes on gray faults with lowercase letters are documented by historical records (Table 3). Faults with Roman numbers are right-lateral strike-slip faults, part of the Median Tectonic Line. The thick dotted line outlines the region analyzed in Figure 9.

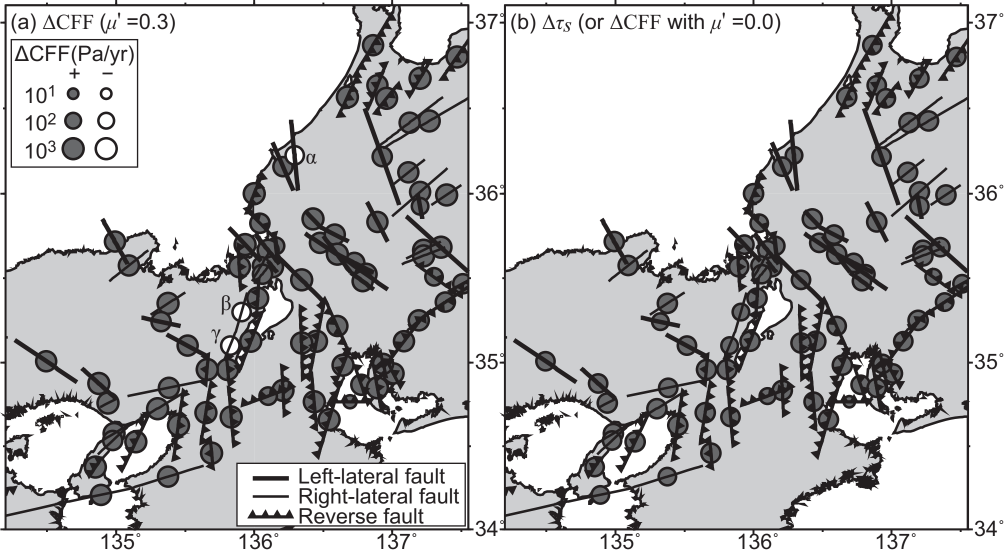

Figure 4. Long-term changes in CFF on inland active faults due to NKTZ east-west compression. Conditions defined for this model were uniform east-west compression with a direction of N100°E and a strain rate of 0.3×10^{-7} year^{-1}. (a) Changes in CFF with apparent coefficient of friction $\mu' = 0.3$. (b) Changes in shear stress, or changes in CFF with apparent coefficient of friction $\mu' = 0.0$. Greek letters correspond to subscript Greek letters in Table 1.

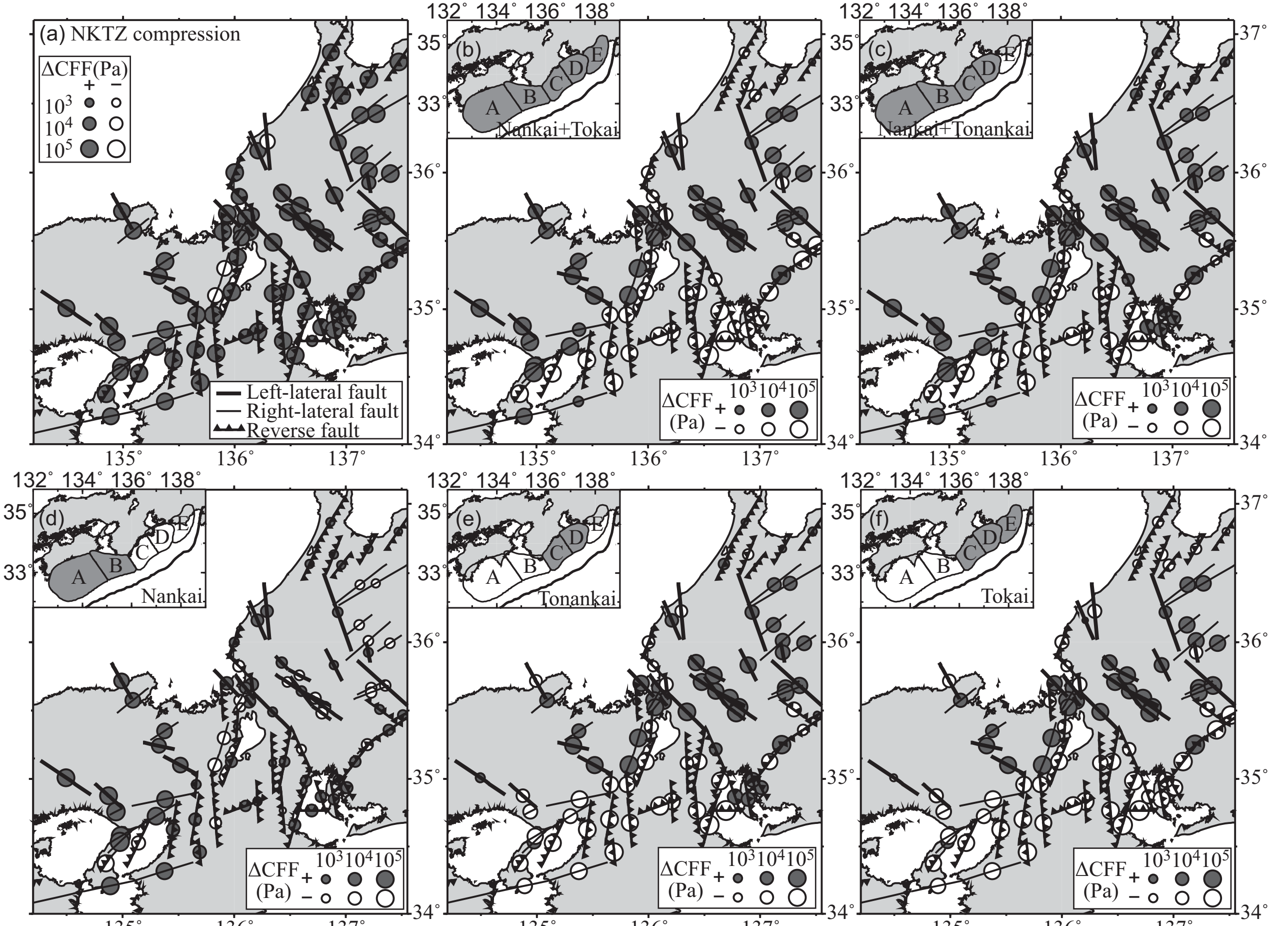

Figure 5. Coseismic changes in CFF on the inland active faults due to interplate earthquakes. The slip regions are (b) ABCDE, (c) ABCD, (d) AB, (e) CD, and (f) CDE, which correspond to the named earthquakes shown in Figure 2. The amount of slip in each region is set at the accumulated slip deficit for 100 years. For comparison, the changes in CFF for 100 years due to NKTZ compression are shown in (a) (the same figure as Figure 4a).

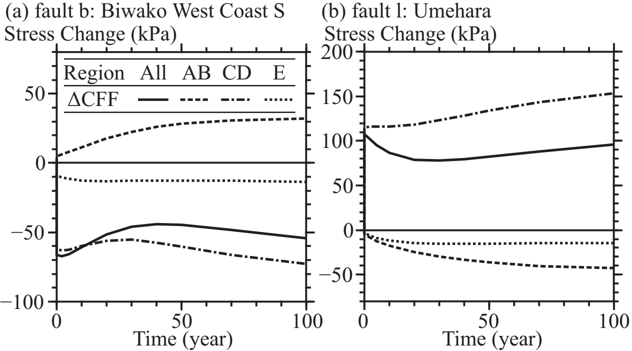

Figure 6. Time evolution of ΔCFF, on (a) a reverse fault b and (b) a strike-slip fault l (Figure 3), due to the interplate earthquakes along the Nankai trough and the following viscoelastic relaxation in the asthenosphere. The amount of slip given in the source regions at the interplate earthquakes is equal to the slip deficit during 100 years.

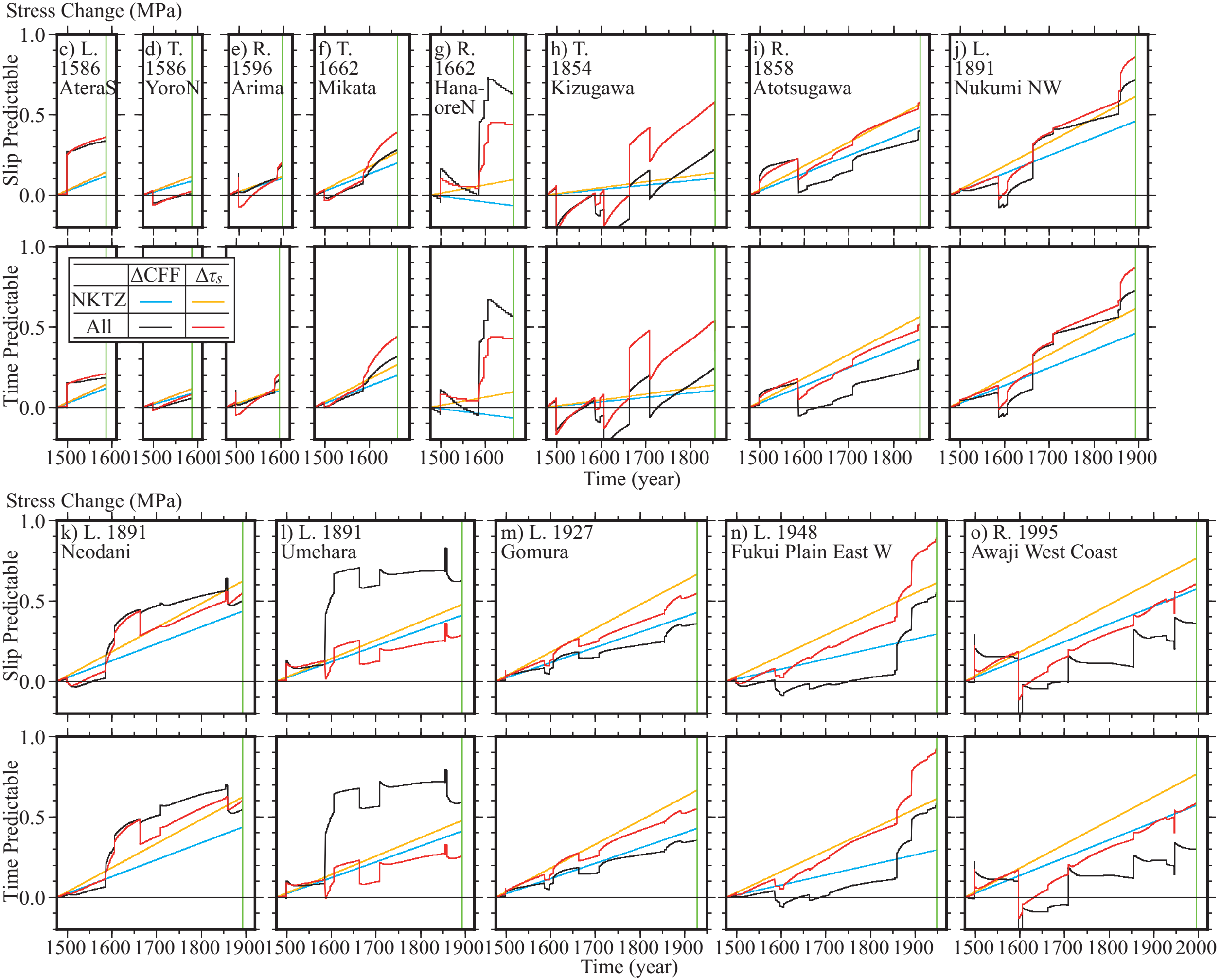

Figure 7. ΔCFF(t) and $\Delta\tau_s(t)$ on the inland active faults with historically recorded earthquakes (Figure 3 and Table 3). ΔCFF(t) and $\Delta\tau_s(t)$ due to all the sources examined in this study (i.e., NKTZ compression, interplate earthquakes, interplate locking, and inland earthquakes) are shown by black and red lines, respectively. ΔCFF(t) and $\Delta\tau_s(t)$ due to only NKTZ compression are shown by light blue and orange lines, respectively. We also show the fault type. Abbreviations for fault types: L, Left-lateral strike-slip; R, Right-lateral strike-slip; T, Reverse fault (Thrust).

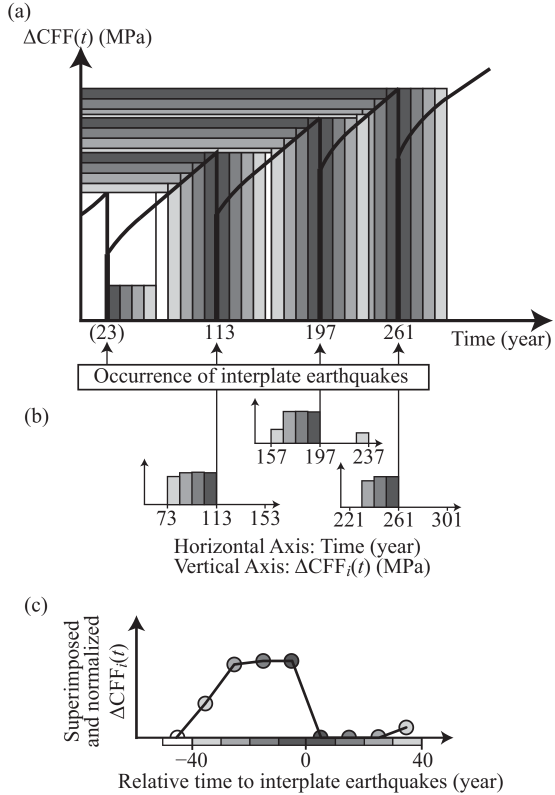

Figure 8. Schematic diagram showing how superimposed and normalized $\Delta CFF_i(t)$ was obtained. (a) Hypothetical $\Delta CFF(t)$ on an idealized inland fault. Different gray levels show the number of years before or since the interplate earthquake along the Nankai Trough, from white (from −50 to −40 years) to dark gray (from −10 to 0 years) and from dark gray (from +0 to +10 years) to light gray (from +30 to +40 years). The thicknesses of bars projected to the left axis show "the increment values of the highest ΔCFF." (b) Temporal change in the increment values of the highest ΔCFF, $\Delta CFF_i(t)$. (c) Temporal change of $\Delta CFF_i(t)$ which is superimposed and normalized. The horizontal axis represents time relative to the occurrence times of the great interplate earthquakes along the Nankai Trough.

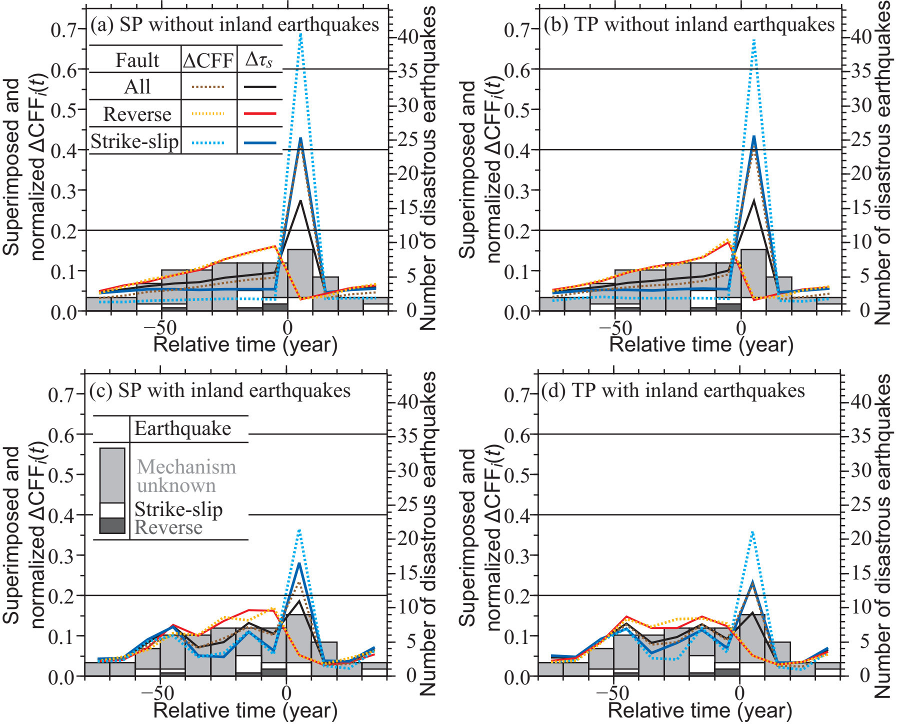

Figure 9. Temporal distribution of the disastrous earthquakes (right axis) and the superimposed and normalized increment values (left axis), $\Delta CFF_i(t)$ (dotted line) and $\Delta\tau_{si}(t)$ (solid line) on inland faults in the region surrounded by the thick dotted line in Figure 3. First, we obtain the superimposed and normalized increment value on each fault, as schematically presented in Figure 8. Then, the obtained values are averaged for examined faults (total number: 73; reverse faults: 29; strike-slip faults: 44). The histogram shows the number of disastrous earthquakes in Table 4. Dark gray and white bars show the reverse and strike-slip earthquakes in Table 3, respectively. The light gray bars show earthquakes not listed in Table 3, but listed in Table 4. The origin of the horizontal axis corresponds to the occurrence years of the Nankai Trough events in region CD.

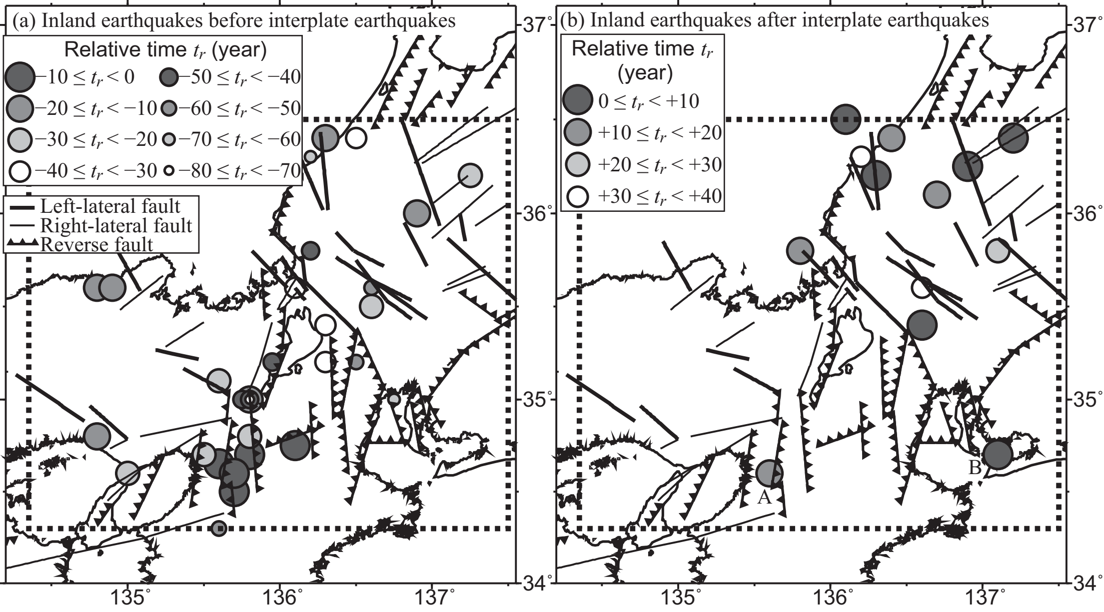

Figure 10. Spatiotemporal distribution of inland earthquakes whose epicentral coordinates are given in Table 4. Thick dotted line shows the region analyzed. Circles of different gray level and size show the relative time t_r to interplate earthquakes. "A" and "B" correspond to the two earthquakes with those letters shown as subscripts in the "Date" column in Table 4.

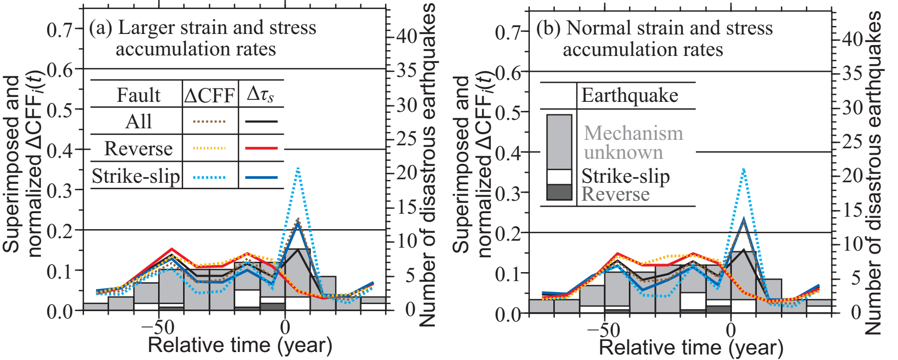

Figure 11. Same as Figure 9d, but under larger strain and stress accumulation rates on inland faults due to the NKTZ compression. Strain accumulation rates $\Delta\varepsilon_{\mathrm{NTKZ}}$ are (a) 0.4×10^{-7} year^{-1} and (b) 0.3×10^{-7} year^{-1}. Figure 11b is shown for comparison (the same figure as Figure 9d).